



# Experimental determination of melt interconnectivity and electrical conductivity in the upper mantle



Mickael Laumonier<sup>a,\*</sup>, Robert Farla<sup>a</sup>, Daniel J. Frost<sup>a</sup>, Tomoo Katsura<sup>a</sup>, Katharina Marquardt<sup>a</sup>, Anne-Sophie Bouvier<sup>b</sup>, Lukas P. Baumgartner<sup>b</sup>

<sup>a</sup> Bayerisches Geoinstitut, University of Bayreuth, Bayreuth, Germany

<sup>b</sup> Institute of Earth Science, University of Lausanne, Geopolis, 1015 Lausanne, Switzerland

## ARTICLE INFO

### Article history:

Received 11 October 2016

Received in revised form 23 January 2017

Accepted 26 January 2017

Available online 20 February 2017

Editor: J. Brodholt

### Keywords:

electrical conductivity

upper mantle

Low Velocity Zone

melt interconnectivity

olivine aggregate

basalt

## ABSTRACT

The presence of a small fraction of basaltic melt is a potential explanation for mantle electrical conductivity anomalies detected near the top of the oceanic asthenosphere. The interpretation of magnetotelluric profiles in terms of the nature and proportion of melt, however, relies on mathematical models that have not been experimentally tested at realistically low melt fractions (<0.01). In order to address this, we have performed *in situ* electrical conductivity measurements on partially molten olivine aggregates. The obtained data suggest that the bulk conductivity follows the conventional Archie's law with the melt fraction exponents of 0.75 and 1.37 at melt fractions greater and smaller than 0.5 vol.% respectively at 1350 °C. Our results imply multiple conducting phases in melt-bearing olivine aggregate and a connectedness threshold at ~0.5 vol.% of melt. The model predicts that the conductive oceanic upper asthenosphere contains 0.5 to 1 vol.% of melt, which is consistent with the durable presence of melt at depths over millions years while the oceanic plates spread apart at the mid-ocean ridge. Beneath ridges a minimum permeability may allow mid-ocean ridge basalts to rise out of the mantle, where our model indicates that melt is present in proportions of up to 4 vol.%.

© 2017 Elsevier B.V. All rights reserved.

## 1. Introduction

One of the most striking geophysical anomalies identified in the upper mantle is the Low Velocity Zone (LVZ, e.g. Holtzman, 2016) characterized by low seismic velocities and high attenuation and located in the asthenosphere near the Lithosphere–Asthenosphere Boundary (LAB). Under oceanic plates, the LVZ appears to coincide in some regions with a 20 to 50 km thick layer that possesses a high electrical conductivity (EC) (up to  $\text{Log } \sigma = -0.3$ ;  $\sigma$  in S/m) relative to overlying and underlying layers (e.g. Evans et al., 2005; Baba et al., 2006; Naif et al., 2013; Sarafian et al., 2015).

Several factors that might enhance EC have been invoked to explain these anomalies, such as anisotropy in mineral conductivity (e.g. Poe et al., 2010), water dissolved in nominally anhydrous minerals (e.g. Dai and Karato, 2014), or the presence of melt (e.g. Gaillard et al., 2008; Yoshino et al., 2010; Ni et al., 2011; Sifré et al., 2014). However, conductivity anisotropy in olivine aggregates appears to have an insufficient effect on EC to account for the observed mantle anomaly (Poe et al., 2010;

Yang, 2012). In addition, water dissolved in olivine is unlikely to produce the conductivity anomalies observed in the upper mantle (Gardés et al., 2014) because the concentration of water in minerals required to reach upper mantle conductivities (100 to 1000 ppm; e.g. Dai and Karato, 2014) would lead to partial melting of the mantle rocks, accompanied by partitioning of significant proportions of water into a melt phase rather than minerals (Hirschmann, 2006). Anisotropic distribution of the melt may also be a further factor enhancing the EC (Caricchi et al., 2011; Zhang et al., 2014; Pommier et al., 2015a, 2015b). For these reasons, it seems that the presence of melt is the most likely explanation for the EC anomalies in the upper mantle, supported by melt–solid viscosity and density contrast (Sakamaki et al., 2013).

Large differences in transport properties between silicate minerals and melt mean that the EC of silicate melts is orders of magnitude higher than mineral phases (e.g. Tyburczy and Fislér, 1995). As a consequence, the bulk EC of partially molten rocks (minerals + melt) varies with the relative fraction of solid and liquid phases, but also with their respective distribution (Glover, 2010 and references therein). A liquid phase should form an interconnected network in a solid aggregate whenever dihedral angles between the two phases are lower than 60°. Since, in olivine aggregates, basaltic melt is distributed as pockets, tubes and films

\* Corresponding author.

E-mail address: mickael.laumonier@gmail.com (M. Laumonier).

**Table 1**

Chemical compositions and standard deviations (italic grey font) of the starting materials (Olivine & Synthesis, whereby the nominal and the analyzed composition of the latter are reported) and melt compositions after experiments. All analyses were normalized to 100 wt.%, and the total (\*) shows the sum of oxides before correction. The number of analyses performed is indicated after the name of each experiment.

#Exp	SiO <sub>2</sub>	TiO <sub>2</sub>	Al <sub>2</sub> O <sub>3</sub>	Cr <sub>2</sub> O <sub>3</sub>	Gd <sub>2</sub> O <sub>3</sub>	FeO	MgO	NiO	MnO	CaO	Na <sub>2</sub> O	K <sub>2</sub> O	Total*
Olivine (54)	39.78 <i>0.75</i>	0.01 <i>0.01</i>	0.02 <i>0.02</i>	0.04 <i>0.07</i>		8.21 <i>0.20</i>	51.37 <i>0.64</i>	0.38 <i>0.05</i>	0.12 <i>0.04</i>	0.06 <i>0.02</i>	0.01 <i>0.01</i>		
nominal	52		15		2	7.5	8.5			10	3	2	100
Synthesis (20)	52.00 <i>0.31</i>	0.01 <i>0.01</i>	15.34 <i>0.19</i>		1.88 <i>0.23</i>	6.81 <i>0.17</i>	8.68 <i>0.17</i>		0.02 <i>0.02</i>	10.20 <i>0.13</i>	3.10 <i>0.10</i>	1.96 <i>0.04</i>	98.71 <i>2.71</i>
M480 – 100% (16)	48.27 <i>0.40</i>	0.01 <i>0.02</i>	14.38 <i>0.35</i>		1.80 <i>0.14</i>	6.15 <i>0.17</i>	13.58 <i>0.96</i>		0.01 <i>0.01</i>	10.43 <i>0.32</i>	3.28 <i>0.16</i>	2.09 <i>0.13</i>	97.75 <i>0.53</i>
M484 – 10% (15)	48.86 <i>0.73</i>	0.03 <i>0.02</i>	12.19 <i>0.82</i>		1.64 <i>0.24</i>	9.59 <i>0.56</i>	11.34 <i>1.62</i>		0.15 <i>0.05</i>	10.98 <i>0.55</i>	3.02 <i>0.22</i>	2.19 <i>0.23</i>	97.98 <i>0.48</i>
M477 – 4% (11)	50.21 <i>1.10</i>	0.04 <i>0.02</i>	15.28 <i>2.62</i>		2.18 <i>0.16</i>	7.31 <i>0.86</i>	8.77 <i>0.93</i>		0.19 <i>0.03</i>	10.67 <i>0.39</i>	3.17 <i>0.06</i>	2.19 <i>0.10</i>	96.69 <i>0.63</i>
M486 – 2% (14)	49.75 <i>0.52</i>	0.07 <i>0.02</i>	11.65 <i>0.79</i>		1.40 <i>0.17</i>	9.76 <i>0.50</i>	11.14 <i>0.83</i>		0.19 <i>0.04</i>	10.82 <i>0.65</i>	3.18 <i>0.36</i>	2.06 <i>0.27</i>	98.48 <i>0.52</i>
M487 – 1% (8)	48.65 <i>2.40</i>	0.11 <i>0.05</i>	11.43 <i>0.76</i>		1.18 <i>0.25</i>	9.50 <i>0.64</i>	13.45 <i>1.23</i>		0.15 <i>0.06</i>	10.79 <i>2.59</i>	3.00 <i>0.43</i>	1.73 <i>0.32</i>	95.90 <i>1.10</i>
M488 – 0.5% (29)	49.90 <i>0.62</i>	0.01 <i>0.01</i>	14.15 <i>0.33</i>		1.76 <i>0.24</i>	8.45 <i>0.38</i>	8.81 <i>0.69</i>		0.08 <i>0.03</i>	12.48 <i>0.67</i>	2.67 <i>0.17</i>	1.69 <i>0.14</i>	97.21 <i>0.91</i>
M501 – 0.5% (4)	52.09 <i>1.10</i>	0.05 <i>0.02</i>	13.54 <i>0.67</i>		1.25 <i>0.14</i>	9.57 <i>0.28</i>	10.93 <i>2.50</i>		0.00 <i>0.00</i>	8.77 <i>1.35</i>	2.47 <i>0.19</i>	1.34 <i>0.12</i>	98.45 <i>0.59</i>
M510 – 0.25% (11)	51.45 <i>1.13</i>	0.05 <i>0.03</i>	10.78 <i>0.70</i>		1.14 <i>0.24</i>	7.83 <i>1.16</i>	15.20 <i>2.22</i>		0.15 <i>0.04</i>	9.31 <i>0.69</i>	2.97 <i>0.37</i>	1.10 <i>0.07</i>	97.42 <i>0.49</i>

with dihedral angles as low as  $\sim 10^\circ$ , melt is expected to be interconnected and thus contributes to a significant increase of the EC even at melt fractions lower than 1% (Cmíral et al., 1998; Yoshino et al., 2009; Faul and Scott, 2006; Garapić et al., 2013).

The conductivity of a partially molten assemblage is generally calculated based on a mathematical model with an assumed mineral and melt geometry. The applicability of such models has, to date, not been experimentally investigated, particularly at very low (<1%) melt fractions, which are likely realistic for the upper mantle. Amongst the numerous mixing laws summarized and described by Glover (2010) and ten Grotenhuis et al. (2005), the conventional and modified Archie's laws appear very suitable for calculating the EC of upper mantle materials in which both solid and liquid phases contribute to the bulk conductivity according to defined exponents. Other models, such as the tubes, cubes, and sphere + models (Grant and West, 1965; Waff, 1974) texturally reproduce a melt-bearing aggregate with a melt fraction >0.05 where pockets (pools) and films wetting grain boundaries are the dominant features of the melt network (Miller et al., 2014). At melt fractions lower than 0.02, the melt principally forms channels residing along grain edges, and can still be interconnected down to very low melt fractions resulting in a potentially poor fit to these models (Garapić et al., 2013; Holtzman, 2016). In spite of the proposed interconnectivity threshold (e.g. Holtzman, 2016), it is expected that the melt raises the bulk conductivity at these low (<0.01%) melt fractions.

Estimates for the amount of melt potentially present in the upper mantle is still quite uncertain due to a lack of experimental verification of models relating the degree of partial melt to the resulting EC, particularly at very low (<1%) melt fractions. In order to find the most adequate mixing law for mantle rocks containing low melt fractions, we have performed *in situ* electrical conductivity measurements on olivine aggregate with melt fraction varying from 0 to 100 vol.% at pressures and temperatures up to 3 GPa and 1430 °C respectively. From the results, we build a model based on the conventional Archie's law, which is valid over a large range

of temperature and melt fraction. Then, we discuss the amount of melt potentially existing in the upper mantle, and its mobility. In addition, we estimate the temperature distribution in the asthenosphere without melt based on the present conductivity measurements of melt-free olivine aggregates.

## 2. Experimental procedure

### 2.1. Starting materials and sample preparation

Natural olivine from a Lanzarote peridotite (Canary Islands, Spain) and synthetic basalt were employed as solid and liquid starting materials respectively. The Lanzarote olivine consists of a single chemically homogeneous population of Fo92 (Table 1). Optical impurity-free olivine grains were crushed and sieved to obtain a maximum grain size of 100  $\mu\text{m}$ . Olivine was used without further treatment (e.g. annealing under special conditions) so as to remain close to natural mantle materials. The basaltic glass was produced by mixing reagent grade oxides and carbonates and fusing the mixture twice in an iron-enriched platinum crucible at 1450 °C and 1 atm for 3 h. The resulting homogeneous glass had a composition similar to that of a Mid-Ocean Ridge Basalt (termed "synthesis", Table 1). Gadolinium was added to the melt (a very incompatible element that concentrates exclusively in the liquid) for neutron tomography observations that are not reported here. The same batch of basalt was used for all experiments. Its liquidus temperature was estimated to be approximately 1270 °C at 1.5 GPa from the melting temperature during synthesis and from EC measurements with the sample with 100% of melt. The glass was then cored to provide starting samples of basalt i.e. for 100% melt fraction experiments, while the rest of the glass was crushed into a fine powder ( $\sim 5 \mu\text{m}$  grain size). This powder was mechanically mixed with olivine grains in order to distribute the glass as homogeneously as possible within the olivine aggregate. Each component was accurately weighed (precision of 0.1  $\mu\text{g}$ ) to achieve the desired melt fraction, assuming very little density variation between room and

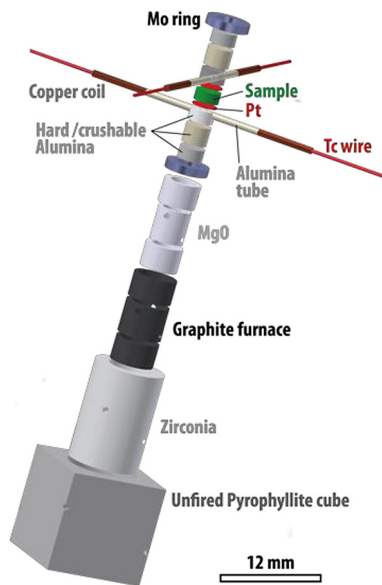


**Fig. 1.** The 12-mm assembly employed for in situ electrical conductivity measurements with the MAVO 6ram press. The sample (green) diameter is 3 mm before compression. The electrical path (red) includes platinum foil electrodes which sandwich the sample and are in contact with 2 S-type thermocouples connected interchangeably to a temperature monitor and a gain phase impedance analyzer. (For interpretation of the references to color in this figure legend, the reader is referred to the web version of this article.)

experimental conditions (Sakamaki et al., 2013). The mixtures are named according to the volume fraction of added basaltic glass (see also section 4.1). The mixtures and the olivine-only aggregate were cold-pressed using a hydraulic press and jig to provide samples 3 mm in diameter and 1.0 to 1.4 mm in length.

## 2.2. In situ electrical conductivity measurements

In every experiment, the sample was placed between two platinum foils (electrodes) in contact with two thermocouples forming the electrical cell (Fig. 1). An MgO sleeve chemically and electrically insulates the sample from the graphite furnace (see Fig. S11). Crushable and hard alumina pistons were placed either side of the sample, which was positioned within the hot zone at the centre of the assembly. This zone extending over  $\sim 1.5$  mm, and was determined by two thermocouples that measured the temperature  $\sim 0.3$  mm away from each edge of the sample. Experiments where a temperature difference larger than  $20^\circ\text{C}$  between the 2 thermocouples was measured, were discarded to avoid EC uncertainties due to large temperature gradients. The furnace and inner parts of the assembly were inserted in a zirconia cylinder used as a ther-

mal insulator that was inserted in an unfired 12-mm edge length pyrophyllite cube. Because of the graphite furnace, the absence of a welded-shut capsule and the presence of olivine, oxygen fugacity is believed to approximate FMQ ( $\pm 1.5$  Log unit) conditions. Confining pressure was applied to the cube by a six-ram press (MAVO press, Bayerisches Geoinstitut) employing second stage anvils with square truncations of 9-mm edge length (Manthilake et al., 2012).

*In situ* EC measurements were performed using a Solartron impedance gain phase analyzer connected to the 4 wires of the 2 thermocouples (see details about impedance spectroscopy in Barsoukov and Macdonald, 2005, for instance). The very low resistance of the liquid basalt required the use of the 4-wire method for accurate EC measurements, as the internal resistance of a 2-wire measurement is significant (see Fig. SI 2). The graphite furnace was heated manually by controlling the electrical power and acted as a grounded Faraday cage, causing only a minor amount of inductive interference in the frequency range 50 to 250 Hz. In a typical run the sample was pressurized for one hour, followed by a heating and cooling cycle, during which impedance spectra were acquired. The 2 thermocouples were switched between the temperature monitor and the impedance spectrometer to avoid interference. After each increase or decrease in temperature the sample was allowed to reach a stable temperature over a period  $\sim 1$  min before the sample resistance was measured. Impedance spectra were typically acquired in a frequency range from 1 MHz to 10 Hz depending on the signal response of the sample and the temperature (Fig. 2). The temperature was monitored before and after the resistance measurement and was generally found to have remained constant. The measurement was repeated when the temperature was found to have deviated by more than  $5^\circ\text{C}$  during the resistance acquisition. Uncertainties on the sample conductivity arise from the sample geometry, temperature measurement and deviation during the measurement and from the determination of the resistance. The total uncertainty calculated by propagating these errors is 0.2 Log units (Laumonier et al., 2015). At the end of the experiment, the furnace power was switched off to quench the sample before slow decompression.

Electrical conductivity mechanisms for minerals and melts have been extensively described in the literature (e.g. Roberts and Tyburczy, 1999; Gaillard, 2004; Yoshino and Katsura, 2010, 2013; Laumonier et al., 2015). It is worth to recall, however, the temperature dependence of the electrical conductivity  $\sigma$  (S/m) according to the Arrhenius Law:

$$\sigma = \sigma_0 \exp^{-(E_a + P \Delta V) / \Re T} \quad (1)$$

where  $\sigma_0$ ,  $E_a$ ,  $P$ ,  $\Delta V$  and  $\Re$  are a pre-exponential term (S/m), the activation energy (J/mol), the pressure (bar), the activation volume ( $\text{cm}^3/\text{mol}$ ) and the gas constant (J/mol/K) respectively.

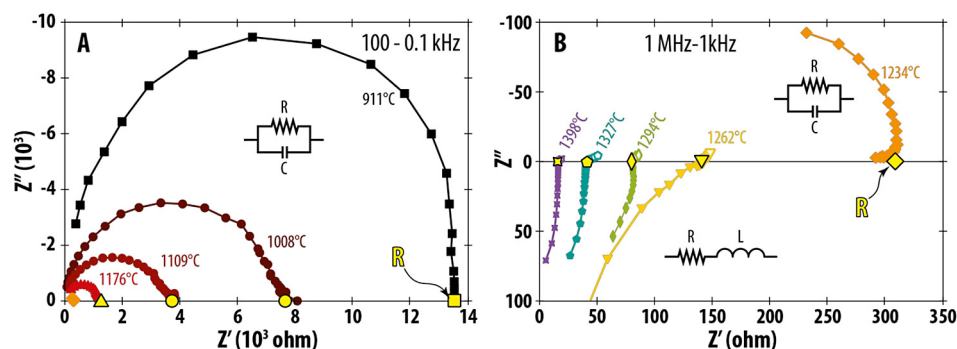


**Fig. 2.** Impedance spectra in the Nyquist plane and equivalent electrical circuits (Huebner and Dillenburg, 1995) obtained at low (A:  $T < 1200^\circ\text{C}$ ) and high (B:  $T > 1200^\circ\text{C}$ ) temperatures on the pure basalt sample. R, C and L in electrical circuits stand for resistance, capacitance and inductance respectively. The real resistance (yellow R) is shown by a yellow symbol. (For interpretation of the references to color in this figure legend, the reader is referred to the web version of this article.)

**Table 2**

Experimental conditions for EC measurements and fitted activation energy  $E_a$  and preexponential factor  $\sigma_0$  (S/m), with standard deviations into brackets.  $T$  °C max to  $T$  °C min defines the temperature interval for the fitting of  $E_a$  and  $\sigma_0$ .

Exp #	Pressure (GPa)	Duration (min)	Added basalt (vol.%)	Geometrical factor ( $10^{-3}$ )	$T$ before quench (°C)	Duration before quench (min)	$T$ max (°C)	$T$ min (°C)	$E_a$ (kJ)	Log $\sigma_0$
M496	1.5	331	0.0	5.90	1348	16	1348	1192	239 (11)	5.84 (0.39)
M502	1.5	203	0.15	4.16	1307	23	1289	1164	163 (3)	3.66 (0.10)
M510	1.5	131	0.25	4.83	1354	21	1360	1182	177 (3)	4.41 (0.09)
M501	3.0	173	0.5	5.09	1299	31	1357	1121	170 (2)	4.60 (0.07)
M488	1.5	399	0.5	2.78	1373	35	1373	1205	162 (5)	4.54 (0.16)
M487	1.5	238	1.0	2.76	1346	102	1430	1292	195 (4)	5.70 (0.14)
M486	1.5	181	2.0	3.24	1373	15	1391	1266	191 (8)	5.80 (0.28)
M478	1.5	308	4.0	1.69	1395	25	1418	1214	207 (4)	6.52 (0.14)
M484	1.5	130	10	2.46	1425	20	1425	1298	206 (4)	6.71 (0.13)
M480	1.5	161	100	3.13	1405	19	1405	1317	210 (2)	7.67 (0.07)
M523	1.5	1690	0.25	6.16	1319	-	-	-	-	-

### 2.3. Post-experiment analysis

Once recovered, the assembly was cut in the middle along an axial plane of the sample, mounted in epoxy resin and polished for textural and chemical analyses. The distribution of the melt and the sample dimensions were characterized by Scanning Electron Microscopy (SEM) with a typical acceleration voltage of 20 to 22 kV. Crystal size distribution and orientation were measured by Electron Backscatter Diffraction on a ZEISS SEM, Leo Gemini 1530 with a Schottky field emission gun employing an accelerating voltage of 20 keV and a beam current of about 2.0–2.5 nA using a 60 mm aperture (more details about the methods in Supplementary Information).

Chemical compositions of melt and minerals (olivine) were quantified by an Electron Probe Micro Analyzer with unfocused (10  $\mu\text{m}$ ) and focused (1  $\mu\text{m}$ ) beams respectively, with an acceleration voltage of 15 kV and beam current of 150 nA. The water content was measured using the Cameca IMS 1280HR at the Swiss SIMS laboratory of the University of Lausanne (Switzerland) under a 10 kV  $\text{Cs}^+$  primary beam with a  $\sim 1.5$  nA current, resulting in a typical spot size of  $\sim 10$   $\mu\text{m}$ . To minimize the water background in the machine, samples were mounted in indium with a reference material. Before each measurement, the surface was cleaned using a 25  $\mu\text{m}$  rastered presputtering beam, for 240 s (more details about the methods in Supplementary Information).

## 3. Results

Table 2 shows the experimental conditions and fitting parameters for the eleven experiments conducted with *in situ* EC measurements. One run was performed at a constant temperature (M523) while all others followed similar heating and cooling cycles. All experiments were carried out at a pressure of 1.5 GPa, except M501 that was conducted at 3 GPa in order to investigate the effect of pressure on EC. The explored melt fraction, based on the initial fraction of added basaltic glass, ranges from 0 (olivine-only) to 100 vol.% (basaltic melt only).

### 3.1. Electrical conductivity of melt-bearing olivine aggregates

The EC of the olivine-only sample (M496) for several heating-cooling cycles is shown in Fig. 3. During the first heating, the EC increased with temperature, corresponding to a low activation energy ( $E_a \sim 50$  kJ/mol), likely due to the presence of moisture up to  $\sim 700$  °C. Between  $\sim 800$  and  $\sim 1230$  °C,  $E_a$  is a factor of two higher than at lower temperatures ( $E_a \sim 100$  kJ/mol) due to hopping (also called small polaron) conduction and potential grain boundary effects (Wanamaker and Duba, 1993; Sakamoto et al., 2002; Yoshino et al., 2009). At temperatures above 1230 °C, high  $E_a$

( $239 \pm 11$  kJ/mol) indicates that ionic conduction (e.g. Yoshino et al., 2009) is the dominant mechanism, although there may still be minor contributions from other mechanisms (see also Gardés et al., 2014).

The conductivity of sample M510 that contained 0.25 vol.% of added basalt is similar to that of pure olivine below the basalt liquidus temperature (1270 °C), but it becomes significantly higher than olivine at temperatures above 1300 °C (Fig. 3). However, during the following cooling and heating cycles, the conductivity remains higher than that for pure olivine, probably due to the better wetting properties of melt once it has overshot the liquidus temperature and distributed through the solid matrix. The effect of crossing the solidus temperature of the basalt is not visible in the experiment involving 0.25 vol.% of added basalt, probably due to the low amount and initial distribution of melt (Fig. 3).

In the case of the sample composed of basaltic melt only (M480), the jump observed around 880 °C during the first heating can be explained by improved contact between sample and electrodes upon relaxation of the glass once the glass transition temperature has been crossed. Around 1090 °C (grey arrow in Fig. 3), the slope suddenly increases from  $74 \pm 9$  to  $248 \pm 10$  kJ, probably coinciding with the solidus temperature of the basalt. The value of 248 kJ has no physical meaning because the basaltic glass may have partly crystallized, and the formed crystals may have gradually melted at these temperatures. The very good reproducibility of the conductivity measurements during the different heating and cooling cycles attests to the accuracy of the measurements and the limited loss of melt from the sample chamber (see also section 4.1).

The logarithmic EC of the pure olivine aggregate and of olivine aggregates containing various fractions of basaltic melt are displayed as a function of reciprocal temperature in Fig. 4. For all melt fractions investigated, the EC increases with the temperature but is clearly very sensitive to the fraction of melt: the higher the melt fraction, the higher the conductivity. For instance, at 1300 °C, the addition of 0.5 vol.% of basaltic melt increases the EC by one order of magnitude compared to the pure olivine aggregate; the addition of 10 vol.% of melt increases the EC by 1.8 log unit, and the pure basalt liquid end-member is by 2.6 orders of magnitude more conductive. These relations are not affected by run duration: experiment M523 was performed at a single temperature of 1319 °C for 27 h, but the conductivity is consistent with data from M510 which contained the same melt fraction but followed a temperature–time cycle similar to the other experiments (Fig. 4; see also Fig SI 3). M488 and M501 both contained a basalt melt fraction of 0.5 vol.% and were conducted at 1.5 and 3.0 GPa respectively have identical conductivities within the error.

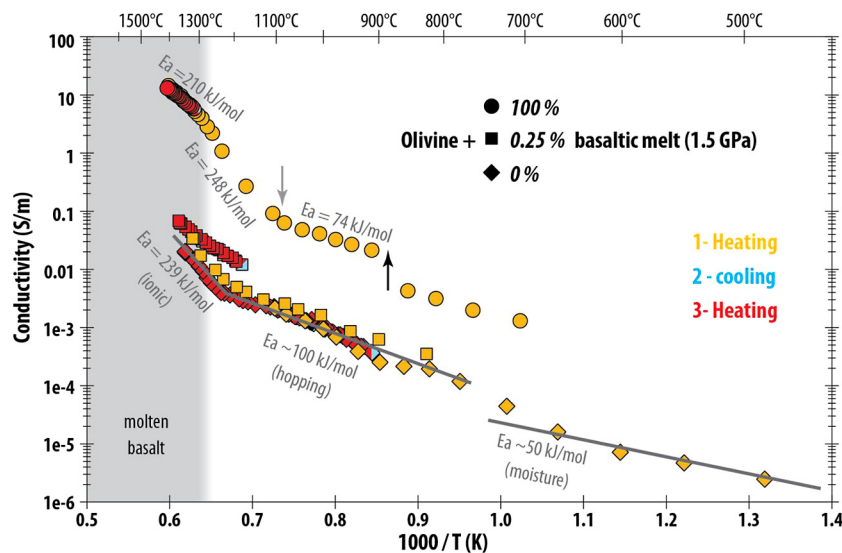


**Fig. 3.** Reciprocal temperature versus electrical conductivity of samples containing 0, 0.25 and 100% of basaltic melt at 1.5 GPa. The activation energy ( $E_a$ ) is indicated for the pure olivine sample, with probable conduction mechanisms. Black and grey arrows correspond to features most likely caused by the glass transition and the solidus of the basalt respectively. The conductivity values obtained during cooling are superimposed by the last heating path. The error in temperature is smaller than the symbols while the maximum error in EC is 0.2 log unit.

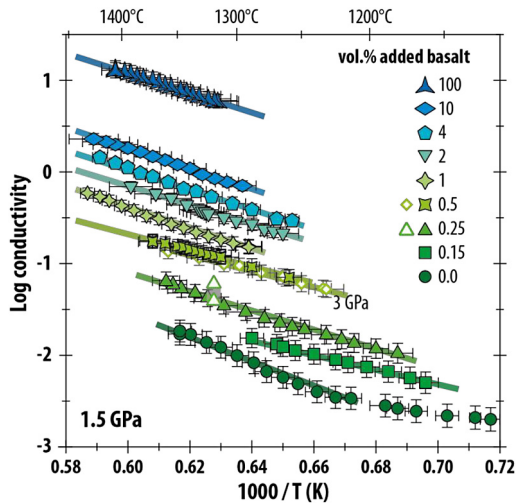


**Fig. 4.** Reciprocal temperature versus EC of basaltic melt and olivine aggregate with 0 to 10 vol.% of added basaltic melt at 1.5 GPa (symbols). An olivine aggregate experiment containing 0.5 vol.% of added basalt was also conducted at 3 GPa (empty diamonds). The range of conductivity measured at constant temperature in experiment M523 is shown by the empty triangles. Lines correspond to the fit of the data using equation (1) and fitting parameters are presented in Table 2.

### 3.2. Textural results

SEM observations of the recovered experimental charges showed that the initial cylindrical shape of the sample was preserved through the experiment with only minor irregularities, mainly where the electrodes are in contact with the thermocouples (Fig. 5; Fig. SI 4). The horizontal cracks observed throughout the sample may have been caused by tensile stresses during decompression and were omitted from the calculation of the geometrical factor (corresponding to the aspect ratio of the sample, *i.e.* the surface divided by the length; Table 2). The grain size ranges up to 100  $\mu\text{m}$ , but shows no significant grain growth over the duration of the experiments (Fig. SI 5). The effect of grain size on EC was not investigated here. Low magnification images show a relatively homogeneous distribution of melt, which is visible as pockets  $\sim 50 \mu\text{m}$  across in the experiment where  $\leq 2$  vol.% of melt was added (Fig. 5 A, C & F). The elongated melt pockets appear

to follow the flow lines typically induced by compressive deformation, *i.e.* sub-normal to the electrodes at the top and bottom of the sample, rotating sub-parallel to the electrodes in the centre of the sample, suggesting a small deviatoric stress was present during the experiments (Fig. 5A and Fig. SI 4C; see more in Section 4.1). At higher magnification, we note the presence of melt as films and tubes, displayed as lines and dots respectively in 2D sections (examples of the labels on Fig. 5B). The melt appears to be fully interconnected for basalt melt fractions  $\geq 2$  vol.% but not interconnected at fractions  $< 0.5\%$  (Fig. 5 D & G). A comparison in the distribution of calcium between experiments with 0.5 and 0.25 vol.% melt contents reveals the presence of small melt-associated Ca-rich pockets in both samples but Ca-rich films are not visible in the sample with 0.25 vol.% of added melt (Fig. 5 E & H).

### 3.3. Chemical composition and water content of experimental products

The chemical composition of olivine after experiments is almost identical to the starting composition (Fig. SI 6). The slight increase of the Fo content, by up to  $\sim 0.01$  (molar  $\text{Mg}/(\text{Fe} + \text{Mg})$ ), is probably related to minor reaction with the MgO capsule (see section 1 of supplementary materials), slight loss of Fe to the Pt electrodes and/or a minor readjustment in mineral/melt Fe–Mg partitioning.

The chemical composition of the melt in the experimental products is similar to that of the starting basaltic melt (Table 1). There is some variation apparent in the concentrations of MgO,  $\text{Al}_2\text{O}_3$ , and FeO and a small variation in the sodium concentration (electrical charge carriers) but none of these differences exceed 10%, except for the experiments with a basalt fraction of 0.5 vol.% that show changes that are slightly larger than this. The chemical compositions and textural observations give no indication that interactions occurred between olivine crystals and melt that could have significantly affected the EC measurements.

The water content measured in olivine is below the detection threshold, thus implying a concentration of water lower than 10 ppm in the solid material, in comparison with the dry forsterite used as a calibration standard. In contrast, the glasses contain substantial amounts of water, with the experiments containing the lower melt fractions producing the most hydrous glasses (Fig. 6). The experiment with no crystals produced a glass with little water (0.1 wt.%  $\text{H}_2\text{O}$ ), slightly more than the starting glass (0.03 wt.%).

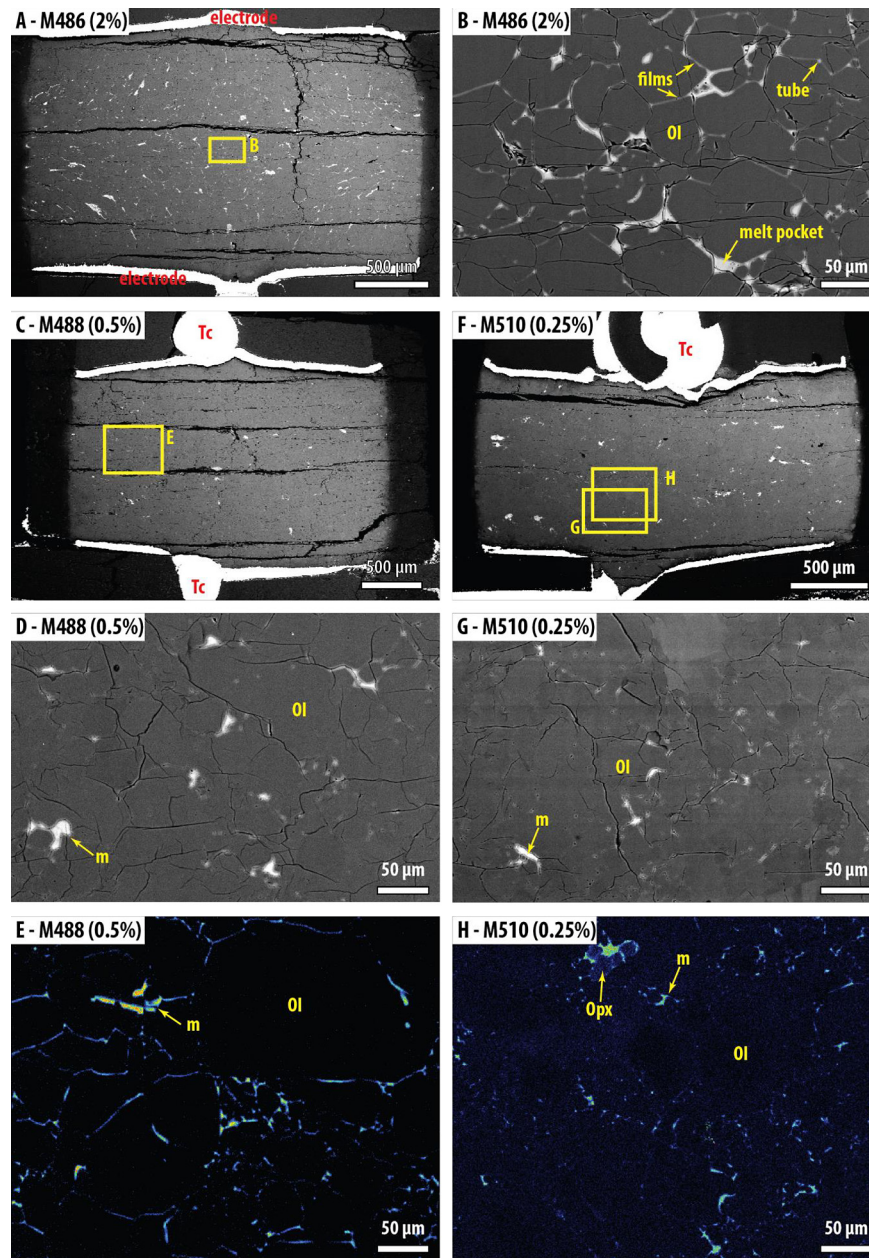


**Fig. 5.** Back-Scattered Electron (BSE) images (A to D, F and G) and relative concentration maps for calcium (E and H) in experiments involving 2, 0.5, and 0.25 vol.% of added basalt. On SEM images, the metal electrodes are white, the melt (m) is light grey and olivine (Ol) is dark grey. Calcium mapping highlights melt pockets and films around olivine crystals (black and dark blue areas). Rare orthopyroxene crystals (Opx) are present at the top of the sample in image H, coming from impurity in the starting material. (For interpretation of the references to color in this figure legend, the reader is referred to the web version of this article.)

Experiments with lower melt fractions resulted in glasses containing between 0.54 wt.% H<sub>2</sub>O (10 vol.% of added basalt) and 0.74 wt.% H<sub>2</sub>O (2 vol.% of added basalt) (Fig. 6). The glasses from the experiments with 0.25, 0.5 and 2 vol.% added melt have similar water contents but there is no clear a correlation between the water content in the experimental glasses and the added melt fraction (Fig. 6).

## 4. Discussion

### 4.1. Experimental limitations

#### 4.1.1. Chemical contamination

The experiments were conducted for durations as short as possible (except M523) in order to limit melt loss or chemical contamination of the sample with the surrounding host assembly. Only

the experiment conducted with pure basaltic liquid (M480) shows a minor amount of melt percolating into the MgO sleeve (Fig. SI 4 A & B). Based on the presence of melt after 27 h at 1319 °C, including regions close to the MgO sleeve, we believe that there is no significant escape of liquid from the sample over the experimental duration. A stable sample volume and EC measurement is, therefore, maintained over the duration of the experiments. The contamination of the sample by the MgO sleeve is limited to a narrow peripheral layer of 100 to 150 μm in the longest duration experiment (excluding M523), representing less than 5% of the sample diameter. On the other hand, the platinum electrodes alloy to some degree with iron from olivine and the melt, the latter remaining homogeneous in composition (see iron distribution in the 100% melt experiment, Fig. SI 4B) except in a narrow (<50 μm) layer at the contact with electrodes. This alloying, however, does not influence the electrical conductivity of the sample.

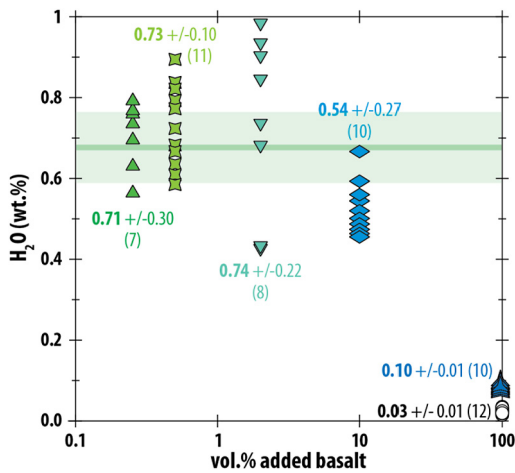


**Fig. 6.** Water contents (bold font) of melts in experimental products reported with the number of analyses (number in brackets). The average water content in melts from experiments with added melt fractions between 0.25 and 0.10 is  $0.68 \pm 0.09$  wt.% (horizontal green line). (For interpretation of the references to color in this figure legend, the reader is referred to the web version of this article.)

#### 4.1.2. Textural equilibrium

Once above the basalt liquidus temperature of the first heating, the EC reaches a value reproduced during later cooling and heating cycles (see the experiment with 0.25 vol.% of basalt, Fig. 3). According to this observation, we conclude that the melt should have promptly percolated through the sample and wetted the electrodes. The examination of the experiment M523 shows that melt pockets are preserved even after 27 h without further wetting of the crystal aggregate (Fig. SI 4K & L). Coaxial strain in the experiments would have favored the percolation of the melt through the aggregate as highlighted by preferentially oriented melt pockets in samples involving 2 and 10 vol.% of added basalt. The melt distribution geometry in the samples is complex and it is not clear how a small amount of coaxial strain would have contributed to enhance the EC in the samples. However, the consistent orientation of these persistent melt pockets parallel to the electrodes (perpendicular to the electrical path) should have not led to an increase in the bulk conductivity of the sample (Zhang et al., 2014).

#### 4.1.3. Melt fraction determination

The determination of post-experimental melt fractions by SEM observation is challenging due to the image resolution, and the conversion from 2D to 3D. Post-experimental melt fraction estimates are usually under-estimated at low magnification due to the difficulty in observing the thin melt films and pockets, particularly for the samples with the lowest melt fractions (Fig. SI 7). On the other hand, at higher magnification, heterogeneity in melt distribution, *i.e.* the presence of scattered melt pockets of different sizes, leads to biased estimates of the melt–crystal ratio. This can lead to errors in the melt fraction determination that are larger than the initial mass ratio of the mixed components. Consequently, though the glass fraction observed in post-mortem SEM pictures is similar to that determined from the initial weight ratio of olivine and basalt in the starting material of each experiment, we rely only on the latter (Fig. 5, Fig. SI 4 and Fig. SI 7). In addition, it is possible that the pure olivine aggregate does not remain melt-free at high temperatures (for instance,  $T > 1350^\circ\text{C}$ ), since the solidus temperature of an olivine aggregate particularly in the presence of even minor amounts of  $\text{H}_2\text{O}$  could easily be over stepped (Hashim, 2016). However, according to Chantel et al. (2016), the very low amounts of melt that could be expected in the pure olivine aggregate (<0.1%) would not wet the grain boundaries, as reflected in the very high EC compared to samples with a low added basalt

fraction (Table 2 and Fig. SI 7) even though intergranular mass transport is strongly influenced by minor amounts of hydroxyl as proven by the work of Gardés et al. (2012). It is shown that activation energy of diffusion in hydrous-saturated grain boundaries is reduced compared to dry grain boundaries.

#### 4.2. Implications of the melt distribution

For experimental durations investigated in this study (<27 h), melt pockets are preserved regardless of the melt fraction (Fig. 5), including when the melt is not fully interconnected (melt fraction <0.5 vol.%). Complete redistribution of a small melt fraction appears to require much longer timescales than employed in the experiments. Similar persistent melt pockets were also observed by Garapić et al. (2013) after 430 h at high temperature. Alternatively, a threshold melt fraction may be required for the complete redistribution of melt pockets, as discussed in the next section. Their stability excludes any textural evolution that would affect the electrical results.

Although tubes are common features in all samples, films on the grain boundaries are not recognized in the samples containing 0.25 vol.% of added basalt or less (Fig. 5). This feature apparently marks the boundary between low degrees of interconnectivity where films are not present and high degrees of interconnectivity where films are present alongside pockets and tubes. The presence of films implies dihedral angles smaller than  $10^\circ$  (Cmíral et al., 1998). Our observations therefore suggest that olivine does not exhibit dihedral angles less than  $10^\circ$  in the presence of very small melt fractions. Furthermore, dihedral angles were observed to be temperature-dependent in melt-bearing olivine aggregates ranging from  $19^\circ$  to  $9^\circ$  between  $1300^\circ\text{C}$  and  $1450^\circ\text{C}$  (Yoshino et al., 2009). In the olivine–basalt system, the disappearance of films with lower melt fraction seems to record the interconnectivity threshold as supported by the EC measurements (see next section). However, our experimental setup does not allow us to distinguish between the individual effects of pockets or films on the bulk conductivity of the partially molten assemblages.

#### 4.3. Choice of the mixing law

The activation energy and pre-exponential factor were determined for each experiment based on an Arrhenius relationship of EC (Eq. (1); Table 2; Fig. 4). The calculated EC values closely reproduce the experimental data (Fig. 4). For the pure olivine aggregate, only data points obtained at temperatures higher than  $1230^\circ\text{C}$  were used to determine the fit, corresponding to temperature where ionic conduction is assumed to be the dominant transport mechanism (Fig. 3 and Section 6 of supplementary materials). The value of the EC fitted at  $1350^\circ\text{C}$  is plotted against the added melt fraction in Fig. 7: from 100 down to 0.5 vol.%, the EC of partially-molten olivine aggregates defines a trend significantly higher than the models commonly used in the literature, such as +Spheres, Tubes, and Cubes models (Grant and West, 1965; Waff, 1974) (Fig. 7), which can be modeled most closely using the Conventional Archie's law (Eq. (2)):

$$\sigma_{\text{bulk}} = \sigma_l \chi_l^m \quad (2)$$

where  $\sigma_{\text{bulk}}$  is the EC of the system,  $\chi_l$  the melt fraction in vol.%,  $\sigma_l$  the EC of the liquid and  $m$  is a measure of how the ratio  $\frac{\sigma_{\text{bulk}}}{\sigma_l}$  varies as a function of melt fraction and degree of interconnection of the melt (Glover, 2010 and references therein). The value  $m$  will be  $<2$  for a well-interconnected liquid phase and it will tend to unity only if the liquid phase is fully interconnected and is the only conductive phase (Glover, 2010). In our case, at  $1350^\circ\text{C}$  and for an added basalt fraction  $>0.5$  vol.% (*i.e.* a high degree

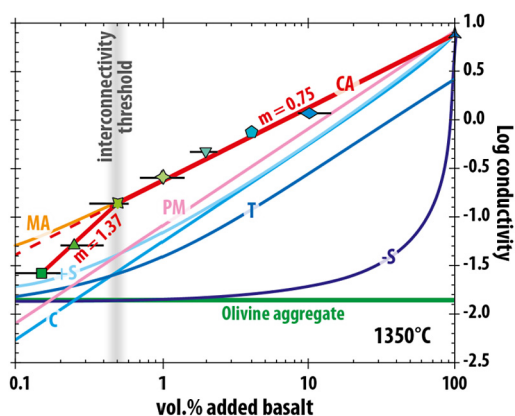


**Fig. 7.** Electrical conductivity versus the fraction of added basalt (in volume %) (Log scale) from the current experimental data (blue to green symbols which are identical to legend of Fig. 4) compared with the Modified Archie's law (MA), Conventional Archie's law (CA), Parallel model (PM), +Spheres (+S), Cubes (C), Tubes (T) and -Spheres (-S) models (curves) from the literature at 1350 °C. See text for model references. Black segments represent the error on the model fraction estimated by image analysis (see supplementary information). (For interpretation of the references to color in this figure legend, the reader is referred to the web version of this article.)

of interconnectivity), the power law exponent  $m = 0.75 \pm 0.02$  while the first term is the conductivity of the basaltic liquid, i.e.  $\log \sigma_l = 0.89 \pm 0.03$  ( $\sigma$  in S/m). This low value of  $m$  indicates that the liquid phase is highly interconnected and that another conduction mechanism contributes to the bulk conductivity so as to provide a value of the exponent  $m < 1$ . The existence of another conduction mechanism than the melt is also demonstrated by the higher EC than given by the parallel model (“PM” in Fig. 7), which is supposed to represent the maximum EC where the melt is the unique conduction mechanism.

The maximum value of  $m$  ( $0.84 \pm 0.05$ ) is obtained when considering the experiments with 0.5 to 2 vol.% of added basalt that contain similar water contents ( $\sim 0.68 \pm 0.09$  wt.%). Based on the experiments of Ni et al. (2011) at 1450 °C, the effect of 1.1 wt.% of water would increase the EC by 0.3 log unit only ( $\log \sigma = 1.0$ ), and the resulting  $m$  exponent would be  $0.86 \pm 0.04$ . Therefore, the value of the exponent  $m$  cannot be the result of the small water content difference observed in the experiments. Since the melt composition does not vary significantly, in particular in the Na content, the reason why the value of  $m$  is lower than unity may reside in the solid phase, even though the EC of the latter is almost 3 log units lower than the basalt melt. Grain boundary effects and/or the existence of an electric double layer (Grahame, 1947) might enhance EC and would argue in favor of a low  $m$  exponent after the Na-coating of crystallizing olivine but these concepts cannot be demonstrated by our experiments.

The  $m$  value we find is comparable to that (0.89) experimentally determined by Yoshino et al. (2010), but significantly different from that calculated by Miller et al. (2015) of  $1.3 \pm 0.3$ . Such a value is inconsistent for melt fractions lower than 0.8% since the conductivity of the melt-bearing olivine aggregate becomes lower than that of olivine-only ( $\log \sigma = -2.05$ ; Constable, 2006). The exponent calculated by Yoshino et al. (2010) on an olivine-carbonatite system ( $m = 1.14$ ) implies a very good interconnectivity, but the existence of one conducting phase only, probably due to the higher conductivity of carbonatite melt compared to a basaltic one (more than one order of magnitude).

#### 4.4. Interconnectivity threshold of the melt fraction (0.5 vol.%)

For experiments with added basalt fractions of 0.25 and 0.15 vol.%, the EC is lower than the trend previously described

(dashed line, Fig. 7) but still higher than the olivine-only aggregate defining a higher exponent of  $m = 1.37$ . We deduce that the basaltic melt is no longer fully interconnected but remains still well-interconnected overall, and still contributes to an increase in the bulk EC. Therefore, under our experimental conditions, an interconnectivity threshold exists at a added basalt fraction of 0.5 vol.% in the olivine aggregates. No mathematical law reproduces such a change in connectedness with the melt fraction. Such a threshold is likely linked to the appearance/disappearance of films, switching to a low/high degree of interconnectivity and resulting in different electrical transport properties. The low degree of interconnectivity is explained by the persistence of tubes in the solid aggregate. The threshold evidenced here occurs at very low melt fraction, and could be easily masked by the high jump in EC observed upon melting observed in other study (e.g. Maumus et al., 2005). The threshold depends on the melt distribution (tubes/films...), thus on the wetting properties of the melt with the solid phase (Yoshino et al., 2009; Zhu et al., 2011).

#### 4.5. Model of the EC of partially-molten olivine aggregate

Since the difference between the conventional and the modified Archie's laws is negligible above the interconnectivity threshold (added basalt fraction  $\sim 0.5$  vol.%), we use the conventional law to fit all data from this study with a high degree of interconnectivity: we now incorporate the temperature dependence on the EC to the previous fit by regressing the evolution of the Archie's law parameters with temperature. The correlation of the two parameters with temperature provides the following simplified equation:

$$\log \sigma = (aT + b) * \log \chi_m + (cT + d) \quad (3)$$

where  $\sigma$ ,  $T$ ,  $\chi_m$  are the electrical conductivity (in S/m), the temperature (in Kelvin) and the melt fraction respectively, and  $a$  to  $d$  are fitting parameters determined from the experiments ( $a = 3.66E-04 \pm 8E-6$ ;  $b = 0.151 \pm 0.013$ ;  $c = 4.52E-03 \pm 1E-4$ ;  $d = -6.448 \pm 0.16$ ). The mixing model integrating both temperature and melt fraction is valid for temperatures higher than 1230 °C and melt fractions  $\chi_m$  higher than 0.5 vol.%.

The same Equation (3) can be applied to calculate the EC of partially molten olivine aggregate with melt fraction ranging between 0.5 down to 0.15 vol.% and temperature higher than 1230 °C. In that case, the fitting parameters are  $a' = 1.57E-04 \pm 4E-6$ ;  $b' = 1.113 \pm 0.006$ ;  $c' = 3.92E-03 \pm 9E-5$ ;  $d' = -4.082 \pm 0.14$ . In this range of melt fraction with a lower degree of connectivity, if  $m = 1.37$ , then the preexponential factor  $A = 2.9$  log units, is a value too high for the conductivity of basaltic melt. Hence, there must be other phase more conductive than olivine to get  $m = 1.37$ , such as, for instance, grain boundary effects that become more and more significant at lower melt fractions (Marquardt et al., 2015).

Both models reproduce very closely the experimental results (see Fig. SI 8) and are compared with data from the literature (Fig. 8) except that for the solid end-member for which the Arrhenius fit is used (Eq. (1); Table 2).

Conductivities for both solid and liquid end-members fall in the range of their respective values defined by previous studies, though most of the melt measurements were performed on basaltic liquids that do not appear to respect an Arrhenius law (Fig. 8) (Presnall et al., 1972; Waff and Weill, 1975; Tyburczy and Waff, 1983; Pommier et al., 2010; Ni et al., 2011). The EC measurements on the pure olivine aggregate reproduce closely those reported for olivine by Poe et al. (2010) along the (100) and (001) axis orientations at lower temperatures ( $T < 1250$  °C) but the data diverge quite significantly at higher temperatures. A comparison between our measurements and those reported for dry olivine and olivine containing 50 ppm of H<sub>2</sub>O (Jones et al., 2012) is consistent with SIMS

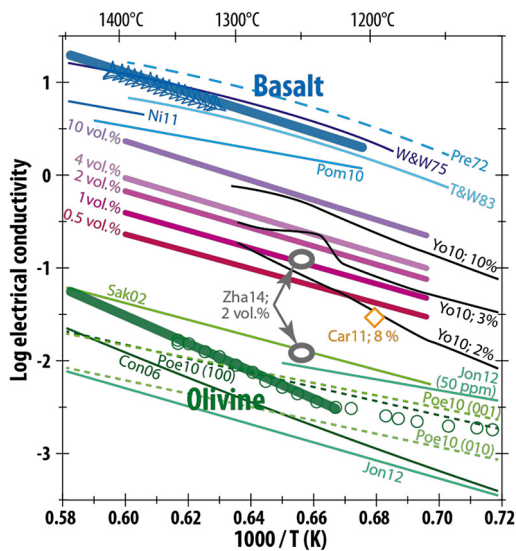


**Fig. 8.** Electrical conductivity plotted against the reciprocal temperature for basalt, olivine aggregate and partially molten olivine aggregates with various fractions of basalt. Thick curves are model end-member conductivities (basalt and olivine aggregate), plotted with the experimental data (3 point stars and circles respectively). Modeled mixtures from this study (purple to pink) are also shown. Previous studies on basalt with comparable compositions are shown as thin blue curves (Presnall et al., 1972; Waff and Weill, 1975; Tyburczy and Waff, 1983; Pommier et al., 2010; Ni et al., 2011), whereas previous olivine measurements are shown by thin green curves (Sakamoto et al., 2002; Constable, 2006; Poe et al., 2010; Jones et al., 2012) and partially molten olivine aggregate measurements (Yoshino et al., 2010; Caricchi et al., 2011; Zhang et al., 2014). The two values from Zhang et al. (2014) correspond to measurement in the direction normal (lower value) and parallel (higher value of conductivity) to the shear direction. Melt proportions from Yoshino et al. (2010) and Caricchi et al. (2011) are expressed in weight %. (For interpretation of the references to color in this figure legend, the reader is referred to the web version of this article.)

analyses indicating  $<10$  ppm  $H_2O$  in our olivine aggregates. Caution should be taken, however, when comparing transport mechanisms determined for single crystals, with those of polycrystalline aggregates since models for this conversion have not been thoroughly tested. Finally, the extrapolation of olivine EC measured at low temperature (typically  $<1200^\circ C$ ) to natural upper mantle conditions by assuming a constant  $E_a$  may be misleading, in particular at low melt fractions and high temperatures where the contribution of olivine to EC is significant.

The comparison of the EC of partially molten olivine aggregate with the study of Yoshino et al. (2010) (10, 3 and 2 wt.% of basalt added to olivine aggregate), corresponding to volume proportions of 8, 2.4 and 1.6 vol.% (when assuming densities of 3.3 for olivine and 2.7 for the basalt), indicate good agreement at  $T < 1300^\circ C$ , but the higher  $E_a$  they found and the presumed absence of water in their experimental products results in lower EC at higher temperatures (Fig. 8). One significant difference between the two studies is the starting grain size (up to 100  $\mu m$  here against a few micrometers in Yoshino et al., 2010). Our model also gives a higher conductivity than deformed partially-molten olivine aggregates (Caricchi et al., 2011; Zhang et al., 2014). In the study of Zhang et al. (2014), the electrical anisotropy of a peridotite with 2 vol.% of basaltic melt was investigated during deformation. The EC in the direction parallel to the shear direction was found to be one order of magnitude higher than in the direction normal to the shear plane. Such a difference comes from the good melt interconnection and agrees with our results (Fig. 8). In addition, if the EC value of the experiment with 2 vol.% of added melt was lowered by one order of magnitude, then this would equate to a melt fraction close to 0.25 vol.%, i.e. in the field of low degree of interconnectivity, such as suggested by Zhang et al. (2014).

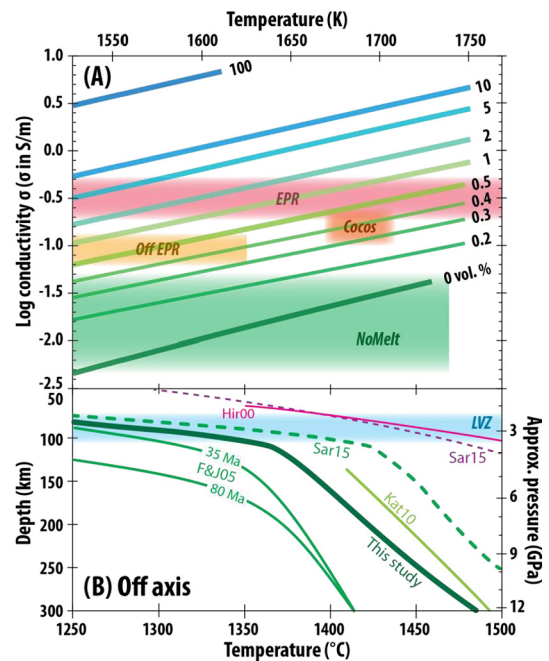


**Fig. 9.** (A) Reported values of electrical conductivity of various upper mantle anomalies: East Pacific Ridge (EPR, Baba et al., 2006), Off axis EPR (Off EPR, Evans et al., 2005; Baba et al., 2006), Cocos plate (Naif et al., 2013) and the NoMelt experiment (Sarafian et al., 2015) compared with the EC of partially molten olivine aggregates (lines, this study) for various plausible basalt fractions (numbers on the right of the lines). The temperature ranges of the Off EPR and NoMelt experiments displayed in the graph are plotted according to a geotherm calculated from the NoMelt depth-conductivity and the olivine-only EC from this study (see section 4.7). (B) Other geotherms from the literature and the approximated depth of the LVZ are plotted for comparison (F&J05: Faul and Jackson, 2005; Kat10: Katsura et al., 2010; Sar15: Sarafian et al., 2015), along with the position of the dry peridotite solidus (Hir00: Hirschmann, 2000; Sar15: Sarafian et al., 2015).

#### 4.6. Estimation of the melt fraction in the upper mantle

##### 4.6.1. Oceanic asthenosphere

Our model for the EC of melt-bearing olivine aggregates can be adapted for the interpretation of melt-induced electrical anomalies located in the upper mantle, in situations where (i) the melt is likely basaltic in composition and exceeds 0.15 vol.%, (ii) assuming the EC of peridotite is similar to that of an olivine aggregate, (iii) the grain size has negligible effect on the EC and (iv) regions are deformed by long-range tectonic stresses. The absence of a measurable pressure effect on the EC between 1.5 and 3.0 GPa implies that the mixing model developed in this study can be applied to understand the conductivity structures of the LAB and LVZ. Our model implies an interpreted maximum melt fraction of 0.4–1 vol.% to explain the conductive, off-axis region of the East Pacific Rise (off EPR), assuming a temperature of  $1350^\circ C$  (Evans et al., 2005; Baba et al., 2006; Sarafian et al., 2015) (Fig. 9A). The lower EC of the Cocos plate LAB ( $\log \sigma = -0.6$  to  $-0.9$  S/m) and higher assumed temperature ( $1420^\circ C$ ; Naif et al., 2013) leads to a melt fraction range of 0.3 to 0.5 vol.%, implying that the melt would not be fully interconnected (Fig. 9A). These melt proportions estimated for the top of the asthenosphere in these two regions are lower than previous estimates (e.g. Evans et al., 1999, 2005; Baba et al., 2006; Hirschmann, 2010; Yoshino et al., 2010; Ni et al., 2011; Naif et al., 2013) as a result of the mathematical models previously employed underestimating bulk EC at low melt fractions. On the other hand, the melt fractions remotely estimated using our model agree with estimates of  $<1\%$  based on melt migration and incremental melting models, in which there is a maximum melt fraction that can be retained by the solid matrix (Kelemen et al., 1997). They also agree with the value of 0.5 vol.%

estimated by Chantel et al. (2016) based on ultrasound velocity measurements.

#### 4.6.2. East-Pacific Rise and Mid-Ocean Ridge regions

The melt fraction estimated beneath the EPR crest will depend strongly on the solidus of the peridotite and, therefore, on the adiabatic gradient. We use a melting depth interval of between 60 and 100 km (Langmuir et al., 1993; Baba et al., 2006; Key et al., 2013) and employ the volatile-poor peridotite solidus determined by Hirschmann (2000) (Fig. 9B) to constrain the pressure (2 to 3 GPa) and temperature (1330 to 1400 °C) of the melting zone beneath the EPR. Under such conditions, based on the conductivity value of Baba et al. (2006) and our results, we estimate melt proportions of between 0.8 and 4 vol.%, which is consistent with the value of Kelemen et al. (1997, and references therein), although less than half the value of 10% proposed by Key et al. (2013).

Contrary to the suggestion of Miller et al. (2015), high concentrations of volatiles in the melt (>0.7 wt%) and olivine aggregate are not required to explain conductive anomalies in the oceanic upper mantle, under ridges or at the top of the asthenosphere. However, higher concentrations of volatiles dissolved in the melt would significantly increase the bulk conductivity (Gaillard, 2004; Ni et al., 2011; Sifré et al., 2014; Laumonier et al., 2015) and the temperature, melt fraction and volatile concentration would be highly correlated. It therefore becomes impossible to resolve between the effects of temperature or volatile concentration using EC alone and some additional constraint needs to be found, a problem that is beyond the scope of this study.

#### 4.7. Temperature estimation of the “NoMelt” upper mantle

Sarafian et al. (2015) reported the EC structure beneath the 70 Ma Pacific plate, located between the Clarion and Clipperton fracture zones where no melt should be present (“NoMelt” experiment). We estimate the temperature distribution of this site using our olivine-only sample conductivity and assuming the absence of melt and significant proportions of volatiles in constituting mantle minerals (Fig. 9A & B). The resulting temperature increases almost linearly from 70 (1265 °C) to 110 km (1362 °C) and from 110 to 300 km (1486 °C) with gradients of ~5°/km and 0.65 °C/km respectively. The temperature profile is about 50 °C lower than the geotherm estimated by Sarafian et al. (2015) that was based on the EC of olivine after Constable (2006); it is similar to that of Katsura et al. (2010) and significantly higher than that proposed by Faul and Jackson (2005) from fitting the shear modulus and attenuation data obtained experimentally on olivine Fo90. The geotherm we calculate implies a temperature difference by about 100 °C from the solidus of dry peridotite (e.g. Hirschmann, 2000; Sarafian et al., 2015). Such a temperature difference excludes the presence of dry, silicate melt in these regions.

#### 4.8. Melt interconnectivity and mobility

The 0.5 to 1% of melt estimated using our model to explain the magnitude of the electrical anomaly at the top of the asthenosphere would have a high degree of interconnectivity but unable to segregate upwards only based on the absence of intense volcanism at the surface. On the contrary, the melt produced beneath a Mid-Ocean Ridge (MOR) rises upwards due to a buoyancy effect, which implies the existence of a minimum permeability threshold for melt ascent in the production of MOR-Basalt, consistent with the efficient draining of the mantle at melt fraction higher than 1% (Zhu et al., 2011). The permeability significantly increases between 0.5–1 vol.% (LVZ) and 0.8–4 vol.% (beneath MOR) without taking into account the anisotropic distribution of the melt. This melt

fraction interval corresponds to a permeability  $k$  (m<sup>2</sup>) bounded between  $\text{Log } k = -16.7$  (at 0.5 vol.% of melt) and  $k = -14.3$  (melt fraction of 4 vol.%) based on Miller et al. (2014). The permeability calculated for a 4 vol.% melt fraction corresponds to a compaction length of the order of 70 km for a MORB-like melt at 1350 °C (McKenzie, 1985), which matches the thickness of the layer the melt has to percolate beneath EPR axis.

The critical melt fraction (melt fraction above which melt is drained through the network, Holtzman, 2016) may thus range between the melt fraction of the LVZ (sustainable melt in the mantle) and the one of intense melt production beneath the MOR. According to our results, such a critical melt fraction in the high conductivity regions ranges between 0.5 and 1 vol.% in volume, significantly higher than 0.1% estimated by Hirschmann (2010). As suggested by Miller et al. (2015), electrical and fluid flow pathways may act differently. The critical melt fraction may also depend on the local and regional stress field. We also still lack knowledge concerning the melt distribution (pervasive or scattered) in natural settings either beneath the MOR or at the LAB. Furthermore, anisotropic distribution of silicate melts may also significantly increase EC (Pommier et al., 2015a). The presence of “petit spot” volcanoes within the oceanic crust might result from localized melt concentrations higher than the critical melt fraction (about 1%) after eventual accumulation, that are thus synonymous with non-pervasive melt distribution in the LVZ, which does not require a formation mechanism that directly involves oceanic plate flexure (Hirano et al., 2006; Yamamoto et al., 2014).

## 5. Conclusions

The results of our *in situ* electrical conductivity measurements allow us to build a model for the electrical conductivity of partially molten olivine aggregates as a function of temperature ( $T > 1230$  °C) and melt fraction (0.15 to 100 vol.%) based on the conventional Archie's Law. The low value of the exponent  $m$  (0.75 at 1350 °C and a melt fraction higher than 0.5 vol.%) suggests that the conductivity of partially-molten olivine aggregate operates through several mechanisms, the main one being achieved by the presence of melt. High volatile concentrations or anisotropic distribution of the melt are not necessarily required in order to explain high conductivities observed in upper mantle settings: we interpret the upper asthenosphere electrical anomaly to result from the presence of 0.5 to 1 vol.% of melt, which is consistent with the persistence of melt at depths. On the other hand, the conductivity of regions beneath MOR results from the presence of higher amounts of melt (<4 vol.%) that ascend towards the crust, thus defining a percolation threshold. Since relatively high concentrations of H<sub>2</sub>O and/or CO<sub>2</sub> have been suggested to be present in the upper mantle (leading to carbonatite melt for the case of CO<sub>2</sub>), our model and conclusions should also be tested on hydrous peridotite and/or carbonatitic melts (Yoshino et al., 2012; Dasgupta et al., 2013; Sifré et al., 2014). In addition, the effect of grain size and thus the grain boundary effects on the electrical conductivity should also be tested, possibly using the approach of Marquardt et al. (2015).

## Acknowledgements

ML was supported by the Alexander von Humboldt Foundation and the free state of Bavaria. KM acknowledges supported by the German Research Foundation (DFG) with grant no MA 6278/2-1 and grant no MA 6278/3-1. We thank H. Keppler, F. Heidelbach, G. Manthilake and E. Gardés for fruitful discussions and the constructive comments from 2 anonymous reviewers. This work would not have been possible without the technical skills of H. Fischer, D. Krause, R. Njul, H. Schulze and S. Übelhack.

## Appendix A. Supplementary material

Supplementary material related to this article can be found online at <http://dx.doi.org/10.1016/j.epsl.2017.01.037>.

## References

- Baba, K., Chave, A.D., Evans, R.L., Hirth, G., Mackie, R.L., 2006. Mantle dynamics beneath the East Pacific Rise at 17°S: insights from the Mantle Electromagnetic and Tomography (MELT) experiment. *J. Geophys. Res., Solid Earth* 111 (B2).
- Barsoukov, E., Macdonald, J.R. (Eds.), 2005. *Impedance Spectroscopy: Theory, Experiment, and Applications*. John Wiley & Sons.
- Caricchi, L., Gaillard, F., Mecklenburgh, J., Le Trong, E., 2011. Experimental determination of electrical conductivity during deformation of melt-bearing olivine aggregates: implications for electrical anisotropy in the oceanic low velocity zone. *Earth Planet. Sci. Lett.* 302 (1), 81–94.
- Chantel, J., Mahtilake, G., Andrault, D., Novella, D., Yu, T., Wang, Y., 2016. Experimental evidence supports mantle partial melting in the asthenosphere. *Sci. Adv.* 2, e1600246.
- Cmíral, M., Gerald, J.D.F., Faul, U.H., Green, D.H., 1998. A close look at dihedral angles and melt geometry in olivine–basalt aggregates: a TEM study. *Contrib. Mineral. Petrol.* 130 (3–4), 336–345.
- Constable, S., 2006. SEO3: a new model of olivine electrical conductivity. *Geophys. J. Int.* 166 (1), 435–437.
- Dai, L., Karato, S., 2014. High and highly anisotropic electrical conductivity of the asthenosphere due to hydrogen diffusion in olivine. *Earth Planet. Sci. Lett.* 408, 79–86.
- Dasgupta, R., Mallik, A., Tsunoi, K., Withers, A.C., Hirth, G., Hirschmann, M.M., 2013. Carbon-dioxide-rich silicate melt in the Earth's upper mantle. *Nature* 493, 211–215.
- Evans, R.L., Tarits, P., Chave, A.D., White, A., Heinson, G., Filloux, J.H., Toh, H., Seama, N., Utada, H., Booker, J.R., Unsworth, M.J., 1999. Asymmetric electrical structure in the mantle beneath the East Pacific Rise at 17°S. *Science* 286 (5440), 752–756.
- Evans, R.L., Hirth, G., Baba, K., Forsyth, D., Chave, A., Mackie, R., 2005. Geophysical evidence from the MELT area for compositional controls on oceanic plates. *Nature* 437 (7056), 249–252.
- Faul, U.H., Jackson, I., 2005. The seismological signature of temperature and grain size variations in the upper mantle. *Earth Planet. Sci. Lett.* 234 (1), 119–134.
- Faul, U.H., Scott, D., 2006. Grain growth in partially molten olivine aggregates. *Contrib. Mineral. Petrol.* 151 (1), 101–111.
- Gaillard, F., 2004. Laboratory measurements of electrical conductivity of hydrous and dry silicic melts under pressure. *Earth Planet. Sci. Lett.* 218 (1), 215–228.
- Gaillard, F., Malki, M., Iacono-Marziano, G., Pichavant, M., Scailliet, B., 2008. Carbonate melts and electrical conductivity in the asthenosphere. *Science* 322 (5906), 1363–1365.
- Garapčić, G., Faul, U.H., Brisson, E., 2013. High-resolution imaging of the melt distribution in partially molten upper mantle rocks: evidence for wetted two-grain boundaries. *Geochem. Geophys. Geosyst.* 14 (3), 556–566. <http://dx.doi.org/10.1029/2012GC004547>.
- Gardés, E., Wunder, B., Marquardt, K., Heinrich, W., 2012. The effect of water on intergranular mass transport: new insights from diffusion-controlled reaction rims in the MgO–SiO<sub>2</sub> system. *Contrib. Mineral. Petrol.* 164 (1), 1–16.
- Gardés, E., Gaillard, F., Tarits, P., 2014. Toward a unified hydrous olivine electrical conductivity law. *Geochem. Geophys. Geosyst.* 15 (12), 4984–5000.
- Glover, P.W.J., 2010. A generalized Archie's law for *n* phases. *Geophysics* 75 (6), E247–E265.
- Grahame, D.C., 1947. The electrical double layer and the theory of electrocapillarity. *Chem. Rev.* 41 (3), 441–501.
- Grant, F.S., West, G.F., 1965. Introduction to the electrical methods. In: Shrock, R.R. (Ed.), *Interpretation Theory in Applied Geophysics*. McGraw-Hill, New York, pp. 385–401.
- Hashim, L., 2016. *Unraveling the Grain Size Evolution in the Earth's Upper Mantle*. PhD, University of Orleans, 124 pp.
- Hirano, N., Takahashi, E., Yamamoto, J., Abe, N., Ingle, S.P., Kaneoka Hirata, T., Kimura, I.J., Ishii, T., Ogawa, Y., Machida, S., Suyehiro, K., 2006. Volcanism in response to plate flexure. *Science* 313 (5792), 1426–1428.
- Hirschmann, M.M., 2000. Mantle solidus: experimental constraints and the effects of peridotite composition. *Geochem. Geophys. Geosyst.* 1 (10).
- Hirschmann, M.M., 2006. Water, melting, and the deep Earth H<sub>2</sub>O cycle. *Annu. Rev. Earth Planet. Sci.* 34, 629–653.
- Hirschmann, M.M., 2010. Partial melt in the oceanic low velocity zone. *Phys. Earth Planet. Inter.* 179 (1), 60–71.
- Holtzman, B.K., 2016. Questions on the existence, persistence and mechanical effects of a very small melt fraction in the asthenosphere. *Geochem. Geophys. Geosyst.* 17 (2), 470–484.
- Huebner, J.S., Dillenburg, R.G., 1995. Impedance spectra of hot, dry silicate minerals and rock: qualitative interpretation of spectra. *Am. Mineral.* 80 (1–2), 46–64.
- Jones, A.G., Fullea, J., Evans, R.L., Muller, M.R., 2012. Water in cratonic lithosphere: calibrating laboratory-determined models of electrical conductivity of mantle minerals using geophysical and petrological observations. *Geochem. Geophys. Geosyst.* 13 (6).
- Katsura, T., Yoneda, A., Yamazaki, D., Yoshino, T., Ito, E., 2010. Adiabatic temperature profile in the mantle. *Phys. Earth Planet. Inter.* 183 (1), 212–218.
- Kelemen, P.B., Hirth, G., Shimizu, N., Spiegelman, M., Dick, H.J., 1997. A review of melt migration processes in the adiabatically upwelling mantle beneath oceanic spreading ridges. *Philos. Trans. R. Soc., Math. Phys. Eng. Sci.* 355 (1723), 283–318.
- Key, K., Constable, S., Liu, L., Pommier, A., 2013. Electrical image of passive mantle upwelling beneath the northern East Pacific Rise. *Nature* 495 (7442), 499–502.
- Langmuir, C.H., Klein, E.M., Plank, T., 1993. Petrological systematics of mid-ocean ridge basalts: constraints on melt generation beneath ocean ridges. In: *Mantle Flow and Melt Generation at Mid-ocean Ridges*, vol. 71, pp. 183–280.
- Laumonier, M., Gaillard, F., Sifre, D., 2015. The effect of pressure and water concentration on the electrical conductivity of dacitic melts: implication for magnetotelluric imaging in subduction areas. *Chem. Geol.* 418, 66–76. <http://dx.doi.org/10.1016/j.chemgeo.2014.09.019>.
- Manthilake, M.A.G.M., Walte, N., Frost, D.J., 2012. A new multi-anvil press employing six independently acting 8 MN hydraulic rams. *Int. J. High Press. Res.* <http://dx.doi.org/10.1080/08957959.2012.680450>.
- Marquardt, K., Rohrer, G.S., Morales, L., Rybacki, E., Marquardt, H., Lin, B., 2015. The most frequent interfaces in olivine aggregates: the GBCD and its importance for grain boundary related processes. *Contrib. Mineral. Petrol.* 170 (4), 40.
- Maumus, J., Bagdassarov, N., Schmeling, H., 2005. Electrical conductivity and partial melting of mafic rocks under pressure. *Geochim. Cosmochim. Acta* 69 (19), 4703–4718.
- McKenzie, D., 1985. The extraction of magma from the crust and the mantle. *Earth Planet. Sci. Lett.* 74, 81–91.
- Miller, K.J., Zhu, W.L., Montési, L.G., Gaetani, G.A., 2014. Experimental quantification of permeability of partially molten mantle rock. *Earth Planet. Sci. Lett.* 388, 273–282.
- Miller, K.J., Montési, L.G., Zhu, W.L., 2015. Estimates of olivine–basaltic melt electrical conductivity using a digital rock physics approach. *Earth Planet. Sci. Lett.* 432, 332–341.
- Naif, S., Key, K., Constable, S., Evans, R.L., 2013. Melt-rich channel observed at the lithosphere–asthenosphere boundary. *Nature* 495 (7441), 356–359.
- Ni, H., Keppler, H., Behrens, H., 2011. Electrical conductivity of hydrous basaltic melts: implications for partial melting in the upper mantle. *Contrib. Mineral. Petrol.* 162 (3), 637–650.
- Poe, B., Romano, C., Nestola, F., Smyth, J.R., 2010. Electrical conductivity anisotropy of dry and hydrous olivine at 8 GPa. *Phys. Earth Planet. Inter.* 181, 103–111.
- Pommier, A., Gaillard, F., Pichavant, M., 2010. Time-dependent changes of the electrical conductivity of basaltic melts with redox state. *Geochim. Cosmochim. Acta* 74 (5), 1653–1671.
- Pommier, A., Leinenweber, K., Kohlstedt, D.L., Qi, C., Garnero, E.J., Mackwell, S.J., Tyburczy, J.A., 2015a. Experimental constraints on the electrical anisotropy of the lithosphere–asthenosphere system. *Nature* 522. <http://dx.doi.org/10.1038/nature14502>.
- Pommier, A., Leinenweber, K., Tasaka, M., 2015b. Experimental investigation of the electrical behavior of olivine during partial melting under pressure and application to the lunar mantle. *Earth Planet. Sci. Lett.* 425, 242–255.
- Presnall, D.C., Simmons, C.L., Porath, H., 1972. Changes in electrical conductivity of a synthetic basalt during melting. *J. Geophys. Res.* 77 (29), 5665–5672.
- Roberts, J.J., Tyburczy, J.A., 1999. Partial-melt electrical conductivity: influence of melt composition. *J. Geophys. Res., Solid Earth* 104 (B4), 7055–7065. <http://dx.doi.org/10.1029/1998JB900111>.
- Sakamaki, T., Suzuki, A., Ohtani, E., Terasaki, H., Urakawa, S., Katayama, Y., Ballmer, M.D., 2013. Ponded melt at the boundary between the lithosphere and asthenosphere. *Nat. Geosci.* 6 (12), 1041–1044.
- Sakamoto, D., Yoshiasa, A., Yamanaka, T., Ohtaka, O., Ota, K., 2002. Electric conductivity of olivine under pressure investigated using impedance spectroscopy. *J. Phys. Condens. Matter* 14, 11375–11379.
- Sarafian, E., Evans, R., Collins, J.A., Elsenbeck, J., Gaetani, G.A., Gaherty, J.B., Lizzaralde, D., 2015. The electrical structure of the central Pacific upper mantle constrained by the NoMelt experiment. *Geochem. Geophys. Geosyst.* 16 (4), 1115–1132.
- Sifré, D., Gardés, E., Massuyeau, M., Hashim, L., Hier-Majumder, S., Gaillard, F., 2014. Electrical conductivity during incipient melting in the oceanic low-velocity zone. *Nature* 509, 81–85.
- Ten Grotenhuis, S.M., Drury, M.R., Spiers, C.J., Peach, C.J., 2005. Melt distribution in olivine rocks based on electrical conductivity measurements. *J. Geophys. Res., Solid Earth* 110 (B12).
- Tyburczy, J.A., Waff, H.S., 1983. Electrical conductivity of molten basalt and andesite to 25 kilobars pressure: geophysical significance and implications for charge transport and melt structure. *J. Geophys. Res., Solid Earth* 88 (B3), 2413–2430.
- Tyburczy, J.A., Fisler, D.K., 1995. Electrical properties of minerals and melts. In: *Mineral Physics and Crystallography: A Handbook of Physical Constants*, pp. 185–208.

- Waff, H.S., 1974. Theoretical considerations of electrical conductivity in a partially molten mantle and implications for geothermometry. *J. Geophys. Res.* 79 (26), 4003–4010.
- Waff, H.S., Weill, D.F., 1975. Electrical conductivity of magmatic liquids: effects of temperature, oxygen fugacity and composition. *Earth Planet. Sci. Lett.* 28 (2), 254–260.
- Wanamaker, B.J., Dube, A.G., 1993. Electrical conductivity of San Carlos olivine along [100] under oxygen- and pyroxene-buffered conditions and implications for defect equilibria. *J. Geophys. Res.* 98 (B1), 489–500.
- Yamamoto, J., Korenaga, J., Hirano, N., Kagi, H., 2014. Melt-rich lithosphere–asthenosphere boundary inferred from petit-spot volcanoes. *Geology* 42 (11), 967–970.
- Yang, X., 2012. Orientation-related electrical conductivity of hydrous olivine, clinopyroxene and plagioclase and implication for the structure of the lower continental crust and uppermost mantle. *Earth Planet. Sci. Lett.* 317–318, 241–250.
- Yoshino, T., Yamazaki, D., Mibe, K., 2009. Well-wetted olivine grain boundaries in partially molten peridotite in the asthenosphere. *Earth Planet. Sci. Lett.* 283, 167–173.
- Yoshino, T., Katsura, T., 2010. Electrical conductivity of mantle minerals: role of water in conductivity anomalies. *Annu. Rev. Earth Planet. Sci.* <http://dx.doi.org/10.1146/annurev-earth-050212-124022>.
- Yoshino, T., Katsura, T., 2013. Electrical conductivity of mantle minerals: role of water in conductivity anomalies. *Annu. Rev. Earth Planet. Sci.* 41, 605–628.
- Yoshino, T., Laumonier, M., Mclsaac, E., Katsura, T., 2010. Electrical conductivity of basaltic and carbonatite melt-bearing peridotites at high pressures: implications for melt distribution and melt fraction in the upper mantle. *Earth Planet. Sci. Lett.* 295 (3), 593–602.
- Yoshino, T., Mclsaac, E., Laumonier, M., Katsura, T., 2012. Electrical conductivity of partial molten carbonate peridotite. *Phys. Earth Planet. Inter.* 194, 1–9.
- Zhang, B., Yoshino, T., Yamazaki, D., Manthilake, G., Katsura, T., 2014. Electrical conductivity anisotropy in partially molten peridotite under shear deformation. *Earth Planet. Sci. Lett.* 405, 98–109.
- Zhu, W., Gaetani, G.A., Fusses, F., Montési, L.G., De Carlo, F., 2011. Microtomography of partially molten rocks: three-dimensional melt distribution in mantle peridotite. *Science* 332 (6025), 88–91.